The Langmuir Circulation Instability as a Mixing Mechanism in the Upper Ocean

SIDNEY LEIBOVICH AND SAMUEL PAOLUCCI[1]

Cornell University, Ithaca, NY 14853

(Manuscript received 7 June 1979, in final form 28 August 1979)

ABSTRACT

A numerical study of the fully nonlinear instability of the ocean to Langmuir circulations is reported. The extended Craik-Leibovich theory is used to compute the development of a mixed layer in an ocean of infinite depth as an initial value problem. A wind stress and surface wave field are imposed on a quiescent ocean with a linear temperature gradient. The initial response to the applied stress is a rectilinear current that is unstable to Langmuir circulations. The resulting convective motions appear to cascade energy from small-scale circulations to more vigorous ones of larger scale. Horizontal averages allow one to identify the Reynolds stress, heat flux and mixing efficiency of the Langmuir "eddies." Mixing efficiencies several times (up to an order of magnitude) larger than those reported in laboratory experiments are possible. It is suggested that numerical experiments such as these may offer a means of parameterizing the effects of sea state and Langmuir circulations for use in one-dimensional and mixed-layer models.

1. Introduction

Langmuir circulations (LC) are large-scale, organized convective motions in the surface layers of the ocean. Surface windrows are visible manifestations of LC that often, but not always, form along the convergence zones of the convection cells. LC are typically of larger horizontal scale than thermally driven convective instabilities, and exist under both thermally stable and thermally unstable conditions. Downwelling velocities approaching 1% of the wind speed and the large scale of LC suggest that this phenomenon can be a powerful mixing mechanism, and of importance in the establishment and maintenance of the mixed layer. The purpose of this paper is to explore the contributions made by LC to the stirring of the mixed layer in quantitative terms. To this end we isolate Langmuir circulations from the collection of possible mixing mechanisms, and calculate the development of a mixed-layer subject to no other mixing process.

In the recent Craik-Leibovich theory (Craik and Leibovich, 1976; Leibovich, 1977a; hereafter denoted as CL and L1, respectively), Langmuir circulations occur due to the interactions of wind-driven currents and surface waves. The theory rests on a set of equations, set out in their fullest form in Leibovich (1977b, hereafter referred to as L2) for the Eulerian mean flow in surface layers under the influence of nearly irrotational surface waves and a surface wind stress. Statically stable or unstable density stratification is allowed for through the Boussinesq approximation. These equations may be derived by the averaging procedure described in L1 or more easily (Leibovich, 1980) from the exact generalized Lagrangian mean equations of Andrews and McIntyre (1978). Surface wave activity leads to a forcing of the mean flow that is felt through a "vortex force" created as a result of vortex line deformation by the wave Stokes drift in a way first described by Leibovich and Ulrich (1972) in a paper that reexamined the Langmuir circulation model originally proposed by Craik (1970). This vortex force may create a torque on the underlying water (see L2) leading to convective activity in either of two ways. One mechanism, explored in CL, L1 and Leibovich and Radhakrishnan (1977) and which we will call CL1, directly forces overturning motions through a surface wave field with a high degree of directional order. The second (or CL2) mechanism (Craik, 1977, L2) produces overturning as a result of an instability of the mean flow created by a vortex force due to waves with *no* special directional properties.

The generalized CL equations (L2) have an "equilibrium" solution consisting of an unsteady unidirectional current [L1, (2.3), (2.4)] and no temperature perturbations. We have studied the global stability and the linear instability of this motion, and the results will be presented elsewhere (Leibovich and Paolucci, 1980a,b). One result of these studies is confirmation that the motion is most unstable to rolls aligned with the applied wind stress; since observed Langmuir circulations are of this form, the result was expected.

[1] Present affiliation: Sandia Laboratories, Livermore, CA 94550.

0022-3670/80/020186-22$09.50

This paper explores the fully nonlinear consequences of the instability mechanism of generating Langmuir circulations in a stratified ocean. The establishment of a mixed-layer structure from an initial uniform (stable) density gradient by means of Langmuir circulation instability is computed from the theory as an initial-value problem. No other mixing mechanisms are invoked. The calculations assume a constant applied wind stress, motion independent of the coordinate aligned with the applied wind stress, and a horizontally homogeneous surface wave field as input. The results of the numerical experiments are detailed time-dependent temperature and velocity fields in the Langmuir cells. Reynolds stresses and buoyancy flux due to the Langmuir circulations are computed from the detailed motion by means of horizontal averages.

Langmuir circulations are reportd to occur when wind speeds exceed 3 m s^{-1} for time durations of several minutes. One presumes, consequently, that their occurrence in the ocean is pervasive, and that most vigorous wind stirring events involve LC as one component. The position, size and motion relative to the water of LC depend on, and are therefore as variable as, the wind and sea state. Thus, in velocity measurements made in the ocean with subrecords averaged over periods of an hour or longer, Langmuir circulations appear as part of the turbulence. In fact, as in the case of the "coherent structures" in turbulent shear flow now being explored experimentally in many laboratories, the occurrence of LC cannot be determined solely from time series of velocity obtained from a single instrument or even from an array of instruments unless the array was especially designed and deployed for this purpose. As in the case of turbulent "coherent structures," identification of LC requires conditional sampling, and visual guidance has been essential.

One-dimensional models of the mixed layer are semi-empirical and depend on laboratory stirring experiments for inputs. Laboratory experiments, however, must underestimate mixing, because large-scale instabilities producing vigorous mixing are excluded in these experiments. This point is made in Turner's (1973) monograph, with specific reference to LC. As an indication of the vigor of LC mixing, our computations show that typical sea state and wind stress conditions produce a mixing efficiency several times that measured by Kato and Phillips (1969).

A theoretical description of LC consistent with field observations of the actual events can therefore supply information for use in one-dimensional models that is otherwise unavailable. In addition to providing information relating mixing to wind forcing, the effects of the sea state, which are important to LC formation, presumably can be parameterized from numerical experiments on a theoretical model of LC such as ours and introduced into one-dimensional models.

The theoretical CL1 model explored in earlier work appears to give results consistent with field observations (L1; Leibovich and Radhakrishnan, 1977) and with laboratory experiments on Langmuir circulations designed to test the CL1 mechanism (Faller, 1978; Faller and Caponi, 1978). The CL2 instability mechanism explored here is based on the same scaling assumptions and therefore, as suggested by Leibovich and Radhakrishnan (1977, p. 484), the general features of the convective cells resulting from both the direct and the instability mechanisms are expected to be similar. The present computations confirm this expectation. Since the instability mechanism does not depend upon any special surface wave organization, it would seem to be the more attractive possibility for Langmuir circulations. It should be noted, however, that the direct forcing mechanism nearly always acts, but may be able to exert a coherent effect only for short periods of time. While this short time duration limits its ability to produce long-lived Langmuir circulation structures, the direct forcing can be expected to lead to initial perturbations that can be subsequently amplified into long-lived Langmuir circulations by the instability mechanism.

In Section 2, the equations and boundary conditions governing the motions we shall study are presented. Four dimensionless parameters, depending on wind stress, surface wave characteristics, turbulent fluid "properties" (where an eddy viscosity assumption has been made) and the initial ambient temperature gradient, appear. These parameters are an inverse Reynolds number, called the Langmuir number following L1, a Prandtl number, a "Richardson number," and a parameter specifying the horizontal width of a convection cell.

The energetics of the convective motion are discussed in Section 3. The finite difference method of solution that we use is presented in Section 4, and numerical results are discussed in Section 5. In numerical experiments such as this, the width of the computational field must be specified *a priori*. One usually expects, however, that a preferred horizontal wavenumber is selected by the instability process. We present detailed calculations for a cell spacing close to the mode Leibovich and Paolucci (1980a) expected to be most unstable according to linear theory, and also for one other choice of width of the computational space. In both cases, convective motions with more than one wavelength initially grow and compete, leading to a changing number of convection cells as the computation advances in time. It appears as though a cascade occurs from small-scale circulations to the largest scale possible in the calculation. Clearly, although the instability characteristics of linear theory select the preferred

mode for marginally unstable systems, they are not useful in the highly unstable regimes considered in this paper, and generally prevailing in the ocean.

A transfer of energy to larger scales was one of the principal conclusions drawn by Faller and Caponi (1978) from their laboratory wind-wave tank experiments on Langmuir circulations. The ultimate size of the cells in the experiments is limited by the water depth, but the trends in the experiments are consistent with trends in the solutions presented here.

Moen (1978) has constructed a model for Langmuir circulations in homogeneous water. We do not believe the model is correct [see Section 3 of Leibovich (1980) for a critique]. Nevertheless, the final equations that he employs have exactly the same mathematical form as the CL equations for constant density water (although the interpretation and parameters are, of course, different). Thus, computations with these equations may be transformed by a suitable scaling into solutions of the CL equations. Moen (1978) has carried out extensive computations similar to the ones presented here, and with similar results. In particular, his calculations also suggest a cascade from smaller to larger scales, although he did not place the same weight on this tendency as we do. Taken together, the two series of computations reinforce each other, and strengthen the evidence for an energy cascade.

2. Equations for wind- and wave-driven convective mixing of stratified water by Langmuir circulations

In this section, the Eulerian-mean equations governing wind-driven motion of stratified water will be recorded. The reader interested in their derivation is referred to Leibovich (1977b).

If we let the positive $\hat{z}$ coordinate point vertically upward, the $\hat{x}$ coordinate point in the wind direction and the $\hat{x}$-$\hat{y}$ plane represent the ocean surface, then in the Boussinesq approximation the motion of the developing currents are described by

$$\nabla\cdot\hat{\mathbf{v}} = 0, \tag{1}$$

$$\frac{\partial\hat{\mathbf{v}}}{\partial\hat{t}} + \hat{\mathbf{v}}\cdot\nabla\hat{\mathbf{v}} = \hat{\mathbf{u}}_s \times (\nabla\times\hat{\mathbf{v}}) - \nabla\hat{\Pi} + \beta g\hat{\theta}\mathbf{k} + \nu_T\nabla^2\hat{\mathbf{v}}, \tag{2}$$

$$\frac{\partial\hat{\theta}}{\partial\hat{t}} + \hat{\mathbf{v}}\cdot\nabla\hat{\theta} = -\hat{w}\bar{T}'(\hat{z}) + \alpha_T\nabla^2\hat{\theta}, \tag{3}$$

with the boundary conditions

$$\left.\begin{aligned} &\frac{\partial\hat{u}}{\partial\hat{z}} = \frac{u_*^2}{\nu_T}, \quad \frac{\partial\hat{v}}{\partial\hat{z}} = \hat{w} = \hat{\theta} = 0 \quad \text{on} \quad \hat{z} = 0 \\ &\hat{\mathbf{v}}, \quad \hat{\theta} \to 0 \qquad\qquad\qquad\quad \text{as} \quad \hat{z} \to -\infty \end{aligned}\right\}, \tag{4}$$

where the carets signify dimensional quantities, and the del operator is understood to be dimensional. In the above, $\hat{\mathbf{v}}$ is the velocity vector, $\hat{\theta}$ is the temperature deviation from the conduction solution $\bar{T}(\hat{z})$ in the motionless fluid, $\hat{\Pi}$ includes the mean kinetic energy of the wave motion per unit volume in addition to the averaged pressure per unit volume, and $\hat{\mathbf{u}}_s$ is the Stokes drift velocity (see Phillips, 1977) defined by the time average (indicated by the angle brackets)

$$\hat{\mathbf{u}}_s = \left\langle \left(\int^{\hat{t}} \hat{\mathbf{u}}_w d\tau \right) \cdot \nabla\hat{\mathbf{u}}_w \right\rangle \tag{5}$$

and arising from averaging the Navier-Stokes equations over the time scale comparable to the period of the surface wave field $\hat{\mathbf{u}}_w$. In Eqs. (2)–(4), u_* is the water friction velocity, β the coefficient of thermal expansion, and ν_T and α_T are the (turbulent) viscosity and thermal diffusivity, respectively; all are assumed to remain constant in time.

The boundary conditions chosen reflect the fact that at the free surface $\hat{z} = 0$, the vertical current vanishes, and the problem of motion developing under the action of an applied wind stress may be treated by imposing the appropriate stress boundary conditions. For water of infinite depth, all disturbances should decay as $\hat{z} \to -\infty$. Finally, thermal boundary conditions must also be imposed on the temperature $\hat{\theta}$. By virtue of the definition of $\bar{T}$, if we assume that the temperature at the surface and at infinite depths is held fixed, then $\hat{\theta} = 0$ at $\hat{z} = 0$ and as $\hat{z} \to -\infty$.

Any suitable boundary condition on

$$\hat{T} = T_r + \bar{T} + \hat{\theta},$$

where T_r is a reference temperature, could have been imposed at the free surface $\hat{z} = 0$. For example, one may have taken a prescribed temperature $\hat{T}_0(\hat{y},\hat{t})$, in which case

$$\hat{\theta}(\hat{y},0,\hat{t}) = \hat{T}_0(\hat{y},\hat{t}) - T_r - \bar{T}(0),$$

or a prescribed heat flux $\hat{T}_0'(\hat{y},\hat{t})$, in which case

$$\frac{\partial\hat{\theta}}{\partial\hat{z}}(\hat{y},0,\hat{t}) = \hat{T}_0'(\hat{y},\hat{t}) - \bar{T}'(0),$$

where

$$\hat{T}_0'(\hat{y},\hat{t}) = \frac{\partial\hat{T}}{\partial\hat{z}}(\hat{y},\hat{z},\hat{t})\Big|_{\hat{z}=0}$$

and

$$\bar{T}'(0) = \frac{\partial\bar{T}}{\partial\hat{z}}(\hat{z})\Big|_{\hat{z}=0}.$$

The chosen boundary condition on $\hat{\theta}$ is therefore one of several physically interesting possibilities.

We assume that the ocean is initially at rest, except for a statistically stationary random surface wave field (or the more elementary case of straight-

crested monochromatic waves) with Stokes drift in the wind direction, and that the mean motion that ensues on application of the wind stress is independent of the wind (x) direction. Thus, we write

$$\hat{\mathbf{v}} = \hat{\mathbf{v}}(\hat{y},\hat{z},\hat{t}) = (\hat{u},\hat{v},\hat{w}), \quad \hat{\theta} = \hat{\theta}(\hat{y},\hat{z},\hat{t}), \tag{6}$$

$$\hat{\mathbf{u}}_s = (\hat{u}_s(\hat{z}),0,0). \tag{7}$$

It is appropriate to nondimensionalize our variables with respect to wave parameters following L1:

$$\left.\begin{aligned} \hat{\mathbf{x}} = \kappa^{-1}\mathbf{x}, \quad \hat{t} = \frac{(\nu_T/\sigma)^{1/2}}{a\kappa u_*}t, \quad \hat{u}_s = a^2\kappa\sigma u_s, \quad \hat{\Pi} = u_*{}^2a^2\left(\frac{\sigma}{\nu_T}\right)\Pi \\ \hat{\mathbf{v}} = \left[\frac{u_*{}^2}{\nu_T\kappa}u, \quad u_*a\left(\frac{\sigma}{\nu_T}\right)^{1/2}v, \quad u_*a\left(\frac{\sigma}{\nu_T}\right)^{1/2}w\right], \quad \hat{\theta} = \kappa^{-1}\bar{T}'(\hat{z})\theta \end{aligned}\right\}. \tag{8}$$

Here u_* is the water friction velocity related to a constant wind stress τ_0 by $\tau_0 = \rho u_*{}^2$, where ρ is a (constant) reference value of the water density; κ is a characteristic wavenumber of the surface wave spectrum; a is a characteristic wave amplitude; and σ a wave frequency scale which is taken to be $(g\kappa)^{1/2}$. It is worth noting at this point that $u_s(z)$ typically decays with depth at least exponentially fast [see Kenyon (1969) for the Stokes drift for a wavefield with arbitrary energy spectrum].

If the dimensionless variables in (8) are introduced in (1)–(3), we obtain

$$\nabla\cdot\mathbf{v} = 0, \tag{9}$$

$$\frac{\partial\mathbf{v}}{\partial t} + \mathbf{v}\cdot\nabla\mathbf{v} = u_s\nabla u + \mathrm{Ri}\,\theta\mathbf{k} - \nabla\Pi + \mathrm{La}\,\nabla^2\mathbf{v}, \tag{10}$$

$$\frac{\partial\theta}{\partial t} + \mathbf{v}\cdot\nabla\theta = -w + \mathrm{La}\,\mathrm{Pr}^{-1}\nabla^2\theta, \tag{11}$$

where the nondimensional parameters arising are the Langmuir number La as defined by Leibovich (1977a) to be

$$\mathrm{La} = \frac{\kappa\nu_T}{au_*}\left(\frac{\nu_T}{\sigma}\right)^{1/2}, \tag{12}$$

a turbulent Prandtl number, defined to be

$$\mathrm{Pr} = \frac{\nu_T}{\alpha_T}, \tag{13}$$

and Ri, a Richardson-number-like parameter, defined to be

$$\mathrm{Ri} = \frac{\beta g\bar{T}'(\hat{z})}{(au_*\kappa)^2}\frac{\nu_T}{\sigma}. \tag{14}$$

The nondimensional boundary conditions are

$$\left.\begin{aligned} &\frac{\partial u}{\partial z} = 1, \quad \frac{\partial v}{\partial z} = w = \theta = 0 \quad \text{on} \quad z = 0 \\ &\mathbf{v}, \quad \theta \to 0 \qquad\qquad\qquad\quad \text{as} \quad z \to -\infty \end{aligned}\right\}. \tag{15}$$

We also note that the dimensionless temperature is now given by

$$T(y,z,t) = \bar{T}(z) + \theta(y,z,t), \tag{16}$$

where we let

$$T \equiv \frac{\kappa(\hat{T} - T_r)}{\bar{T}'}, \quad \bar{T} \equiv \frac{\kappa\bar{T}}{\bar{T}'}.$$

Since the temperature was nondimensionalized with respect to the conduction temperature gradient, the surface temperature can be arbitrarily fixed.

A solution to the above problem subject to zero initial conditions is (cf. Leibovich, 1977a)

$$\left.\begin{aligned} &\bar{\mathbf{v}}(z,t) = 2\left(\frac{\mathrm{La}\,t}{\pi}\right)^{1/2}[\exp(-\eta^2) - \pi^{1/2}\eta\,\mathrm{erfc}(\eta)]\mathbf{i} = \bar{u}\mathbf{i}, \quad \eta = -\frac{z}{2(\mathrm{La}\,t)^{1/2}} \\ &\nabla\bar{\Pi} = u_s\nabla\bar{u}, \quad \bar{\theta} = 0 \end{aligned}\right\}. \tag{17}$$

Actually, any transient solution of the one-dimensional unsteady heat equation in $-\infty < z \leq 0$ can be taken for $\bar{\theta}$; the choice in (17) is obviously the simplest possibility. To analyze the stability of (17) numerically, one can superimpose a disturbance to the above solution at any time $0 < t < +\infty$, and trace its growth (or decay) in time.

A quantity of physical interest is the heat flux across the ocean surface. This is measured in dimensionless form by the Nusselt number Nu, which is the ratio of the actual heat flux to that caused by conduction alone; if there is no convection, Nu = 1. The local value of the Nusselt number at the surface is given by

$$\mathrm{Nu}_0 = 1 + \left.\frac{\partial\theta}{\partial z}\right|_{z=0}. \tag{18}$$

3. Energetics

In this section, we briefly consider the sources and sinks of mixing energy in the fluid, and introduce

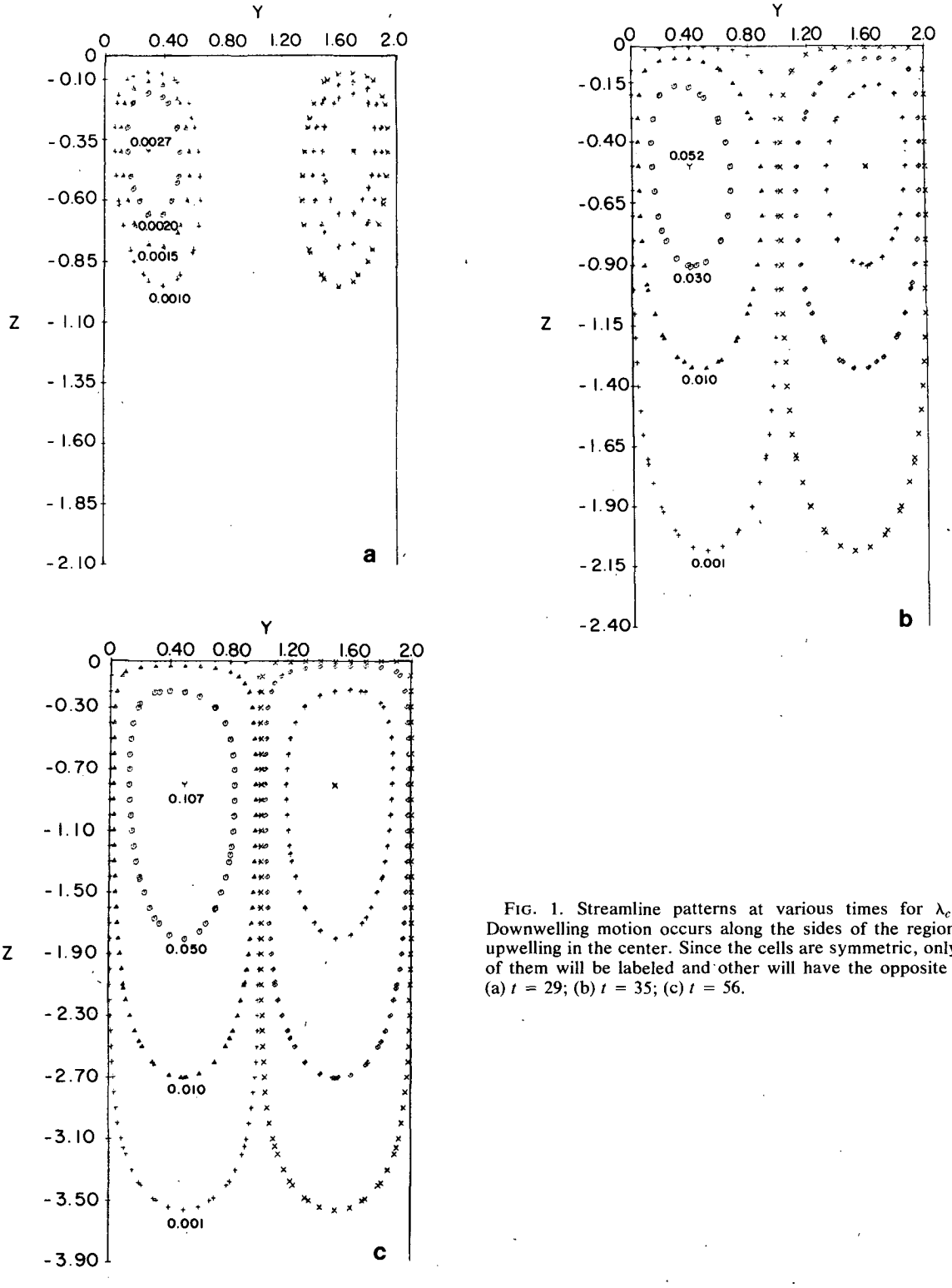

FIG. 1. Streamline patterns at various times for $\lambda_c = 2$. Downwelling motion occurs along the sides of the region and upwelling in the center. Since the cells are symmetric, only one of them will be labeled and other will have the opposite sign. (a) $t = 29$; (b) $t = 35$; (c) $t = 56$.

horizontal averages that will be later extracted from the detailed numerical experiments.

We suppose that the motion is periodic in the cross-wind (y) direction with wavelength λ_y. We need not restrict ourselves in this section to motion independent of the wind (x) direction; if we allow for x variations, however, we require that they also be periodic with a finite period λ_x. If the scalar product of the

momentum equation (2) with the velocity vector $\hat{\mathbf{v}}$ is formed, the resulting equation integrated over a period in y and x (or over a unit x distance in the case of x independent motion) and over the entire water column $-\infty < z < 0$, and boundary conditions (4) applied, the result is

$$\frac{dK}{dt} = \int_V \rho g\beta\hat{w}\hat{\theta}d\mathbf{x} + \int_S \tau_0\hat{u}(x,y,0,t)dxdy - \int_V \rho\hat{u}\hat{w}\frac{d\hat{u}_s}{dz}d\mathbf{x} - D,$$

where K is the kinetic energy of the mean motion

$$K = \tfrac{1}{2}\int_V \rho\hat{\mathbf{v}}\cdot\hat{\mathbf{v}}d\mathbf{x}$$

and D is the dissipation rate to the turbulence and eventually to heat,

$$D = \int_V \rho\nu_T\nabla\hat{\mathbf{v}}:\nabla\hat{\mathbf{v}}d\mathbf{x}.$$

Also V is the fluid volume over which the integration is taken, τ_0 the (assumed constant) surface wind stress, and S the horizontal rectangular surface with sides λ_x and λ_y. We note that the rate of increase of potential energy, PE, of the system is

$$\frac{d}{dt}\text{PE} = -\int_V \rho g\beta\hat{w}\hat{\theta}d\mathbf{x} \tag{19}$$

so the rate of increase of mechanical energy of the mean motion

$$E = K + \text{PE}$$

is described by

$$\frac{dE}{dt} = \int_S \tau_0\hat{u}dxdy - \int_V \hat{u}\hat{w}\frac{d\hat{u}_s}{dz}d\mathbf{x} - D. \tag{20}$$

According to (20) the increase in kinetic and potential energy of the ocean is due to (i) the rate of work done at the surface directly by the wind stress τ_0 on the mean current; (ii) the rate of energy extracted by the mean current Reynolds stresses from the surface waves, as represented by $\hat{u}_s$; and (iii) a decay due to transfer of energy to turbulence and heat through D. We note, in particular, that the Langmuir circulations draw energy from the wind in two ways, one directly as in (i), and the other from the waves which, if they are to be maintained (as assumed here), must extract energy from the wind at a rate sufficient to compensate for the loss to the LC. It turns out, however, that the rate of energy transfer from the wind to the LC via the waves is very small compared to the direct power deposition by the wind to the mean current.

If the momentum and heat equations are integrated only over the horizontal rectangle S indicated above,

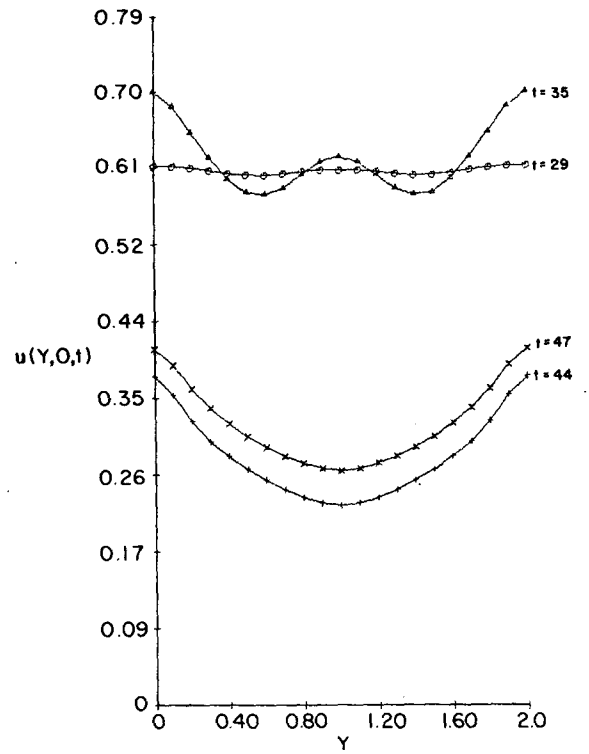

FIG. 2. The wind-directed current speed at the surface as a function of the spanwise coordinate y for different values of time.

the result normalized by the integration area, and the operation indicated by an overbar

$$(\bar{\ }) = \frac{1}{\lambda_x\lambda_y}\int_0^{\lambda_x} dx \int_0^{\lambda_y} (\ )dy, \tag{21}$$

the results are

$$\frac{\partial\bar{\hat{\mathbf{v}}}}{\partial t} + \frac{\partial}{\partial z}\overline{(\hat{w}\hat{\mathbf{v}})} = \overline{\left(\hat{u}_s\frac{\partial\hat{u}}{\partial z} + g\beta\hat{\theta} - \frac{\partial\hat{\pi}}{\partial z}\right)}\mathbf{k} + \nu_T\frac{\partial^2\bar{\hat{\mathbf{v}}}}{\partial z^2}, \tag{22}$$

$$\frac{\partial\hat{\theta}}{\partial t} = \alpha_T\frac{\partial^2\hat{\theta}}{\partial z^2} - \frac{\partial}{\partial z}\overline{\hat{w}\hat{\theta}}. \tag{23}$$

Continuity implies

$$\bar{\hat{w}} = 0 \tag{24}$$

and the stress boundary conditions imply $\bar{\hat{v}} = 0$. Thus, Eq. (22) reduces to

$$\frac{\partial\bar{\hat{u}}}{\partial t} = \nu_T\frac{\partial^2\bar{\hat{u}}}{\partial z^2} - \frac{\partial\overline{\hat{u}\hat{w}}}{\partial z} \tag{25}$$

and

$$\frac{\partial\bar{\hat{\pi}}}{\partial z} = \hat{u}_s\frac{\partial\bar{\hat{u}}}{\partial z} + g\beta\hat{\theta}. \tag{26}$$

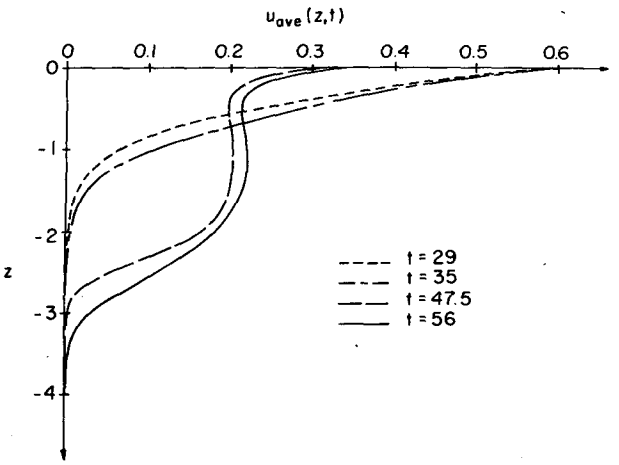

FIG. 3. Average profile of the wind-directed current speed as a function of depth and time. The average is taken over a wavelength λ_c corresponding to the streak spacing.

In Section 5, we shall report computed values of the heat flux

$$q_h = -\overline{\hat{w}\hat{\theta}} \tag{27}$$

(or buoyancy flux $\beta g q_h$) and the Reynolds stress

$$-\overline{\hat{u}\hat{w}} \tag{28}$$

resulting from Langmuir circulation "fluctuations."

The mixing efficiency m is defined in the literature in various ways, depending on what measure of the power input of the wind is used. Here m will be defined to be

$$m = \frac{d}{dt}(\mathrm{PE})(\rho u_*^3 \lambda_x \lambda_y)^{-1}$$

$$= -\rho\beta g \int_{-\infty}^{0} q_h d\hat{z}/\rho u_*^3. \tag{29a}$$

If the dimensionless variables (8) are used to evaluate q_h, the result is

$$m = a\kappa^{-2}\left(\frac{\sigma}{\nu_T}\right)^{1/2} \frac{\beta g \bar{T}'}{u_*^2} \int_{-\infty}^{0} -\overline{w\theta} dz. \tag{29b}$$

For the initial value problem of the kind that we have posed here, m is a function of time, and sample values are given in Section 5. We add here that for an infinitely deep ocean, the neglect of Coriolis acceleration implies that the applied surface stress is always unbalanced. This implies that the momentum in the wind direction must always increase, and that a steady state cannot be attained. Consequently, m need not have a steady limit.

4. Finite-difference approximation of the model equations

In order to examine the stability of the basic solution (17) to roll motions numerically, it is convenient to introduce a streamfunction ψ and the x component of vorticity ξ. In these variables Eqs. (9)–(11) and boundary conditions (15) are

$$\frac{\partial u}{\partial t} = -\nabla\cdot(u\mathbf{v}) + \mathrm{La}\,\nabla^2 u, \tag{30a}$$

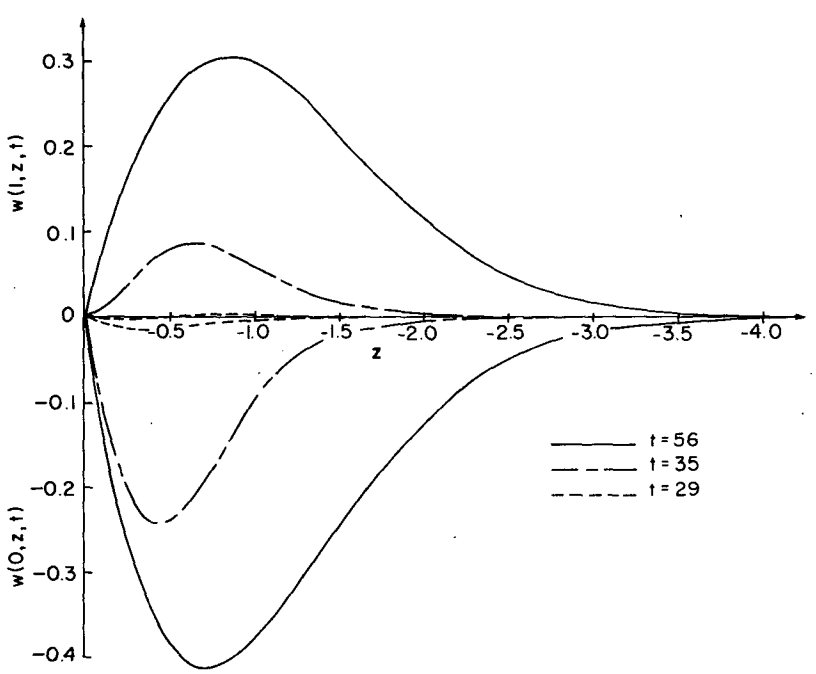

FIG. 4. Vertical velocity component as a function of depth at planes of convergence ($y = 0$) and divergence ($y = 1$) at various times.

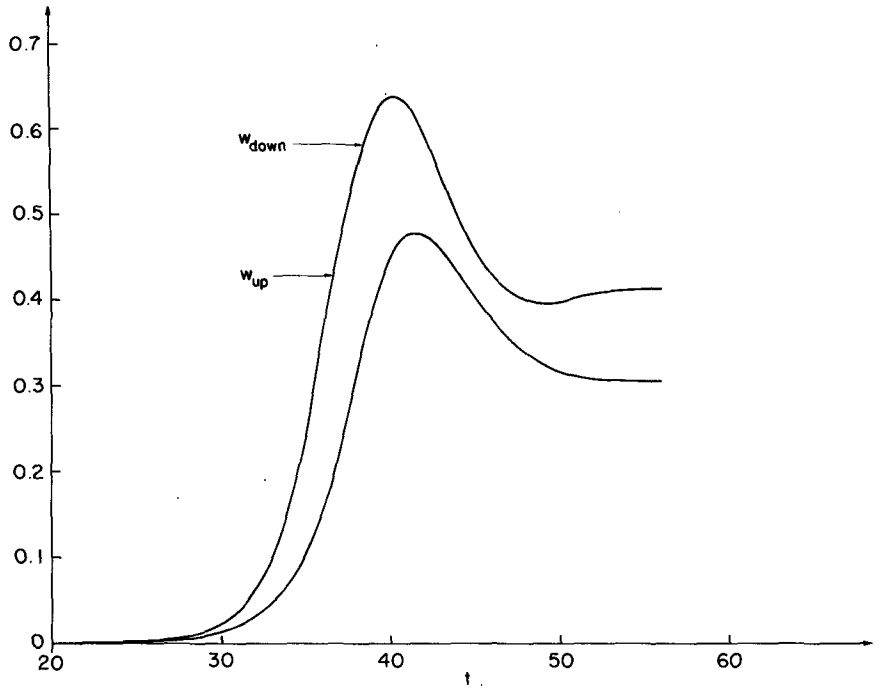

FIG. 5. Maximum upwelling and downwelling speeds as functions of time; $w_{up} = \max_z w(1,z,t)$ and $w_{down} = \max_z |w(0,z,t)|$.

$$\frac{\partial \xi}{\partial t} = -\nabla\cdot(\xi \mathbf{v}) + \mathrm{La}\,\nabla^2\xi + F(y,z,t), \quad (30b)$$

$$\frac{\partial \theta}{\partial t} = -\nabla\cdot(\theta \mathbf{v}) + \mathrm{La}\,\mathrm{Pr}^{-1}\nabla^2\theta - w, \quad (30c)$$

$$\nabla^2\psi = -\xi, \quad \xi = \frac{\partial w}{\partial y} - \frac{\partial v}{\partial z}, \quad (30d,e)$$

$$v = \frac{\partial \psi}{\partial z}, \quad w = -\frac{\partial \psi}{\partial y}, \quad (30f,g)$$

where

$$F(y,z,t) = -\frac{du_s}{dz}\frac{\partial u}{\partial y} + \mathrm{Ri}\,\frac{\partial \theta}{\partial y}, \quad (30h)$$

$$\frac{\partial u}{\partial z} = 1, \quad \xi = \psi = \theta = 0 \quad \text{on} \quad z = 0, \quad (30i)$$

$$u = \xi = \psi = \theta \to 0 \quad \text{as} \quad z \to -\infty. \quad (30j)$$

In anticipation of the solution (17) being unstable and this instability leading to motions periodic in the y direction, symmetry boundary conditions are imposed:

$$\frac{\partial u}{\partial y} = \xi = \psi = \frac{\partial \theta}{\partial y} = 0$$

on

$$y = 0 \quad \text{and} \quad y = d. \quad (31)$$

Here d will correspond to some multiple of one-half the wavelength of the emerging periodic solution. The above problem is not closed, since the width d of our region, or more precisely a preferred wavelength λ_c, remains to be determined. How λ_c must be chosen will be discussed later.

Since it is expected that instability will arise from perturbing the current speed to make it depend on the spanwise coordinate, we choose to perturb the windward velocity component u, and take the disturbance to be independent of the x direction.

The model equations (30a–h) and boundary conditions (30i,j) and (31) are approximated using finite differences central in space and forward in time. For the convective terms the second upwind differencing method is used (see Roache, 1976). The numerical scheme of Leibovich and Radhakrishnan (1977) was easily adapted with the addition of the energy equation and the buoyancy term in the vorticity equation. The computer program was modified to be more machine efficient. The finite-difference equations along with the sequence of computations are listed in Paolucci (1979).

The original scheme of Leibovich and Radhakrishnan (1977) was not fully conservative because the finite-difference approximation of the free-surface boundary condition was not conservative. A conservative equation holding at this boundary was derived using a control volume approach. The derivation is given in Paolucci (1979).

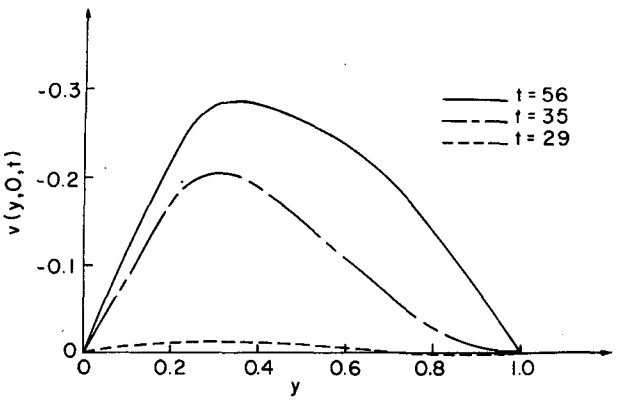

FIG. 6. Surface values of the spanwise (sweeping) velocity component as a function of the spanwise coordinate for different time levels.

The upwind differencing scheme introduces an artificial viscosity. The error due to this artificial viscosity was shown by Runchal and Wolfshtein (1969) to be negligible for two-dimensional driven cavity flows. Since our flow is independent of the x coordinate, and roll circulation is expected, then at any time we essentially have a two-dimensional cavity flow, and the error introduced from the artificial viscosity is expected to be negligible in our case also. The resulting scheme is then in some sense second-order accurate in space and first-order accurate in time, and is conservative and satisfies the transportive property as described by Roache (1976).

The Poisson equation in (29d), which Leibovich and Radhakrishnan (1977) solved using optimized successive overrelaxation, is now solved using an efficient non-iterative exact numerical scheme utilizing the Buneman variant of cyclic reduction. The program used was developed by Swarztrauber and Sweet (1975) at NCAR. Here, as in Leibovich and Radhakrishnan (1977), the condition

$$\frac{\partial \psi}{\partial z} - \frac{d}{\pi}\psi = 0 \tag{33}$$

is applied at the finite lower boundary, since it was shown that for any fixed depth the above condition was more appropriate and gave more accurate numerical results than by applying $\psi = 0$ there.

It is noted that the shear solution (17) has a singularity at $t = 0$. Hence, the numerical calculations had to be started away from this singularity. By setting the Stokes drift velocity u_s to zero, the solution was recovered with very good accuracy with spatial increments $\Delta y = \Delta z = 0.1$, by imposing the appropriate initial conditions [obtained from the analytical solution (17)] at a time slightly away from $t = 0$, e.g., $t = 1$.

All of our results have been obtained for La $= 0.01$, with the grid size $\Delta y = \Delta z = 0.1$, and with time step Δt such that it satisfied the numerical stability requirement

$$\Delta t \leq \left\{\frac{2\mathrm{La}}{S}\left[\frac{1}{(\Delta y)^2} + \frac{1}{(\Delta z)^2}\right] + \frac{1}{4\Delta y}(v_R + |v_R| - v_L + |v_L|) + \frac{1}{4\Delta z}(w_R + |w_R| - w_L + |w_L|)\right\}^{-1}, \tag{34}$$

where

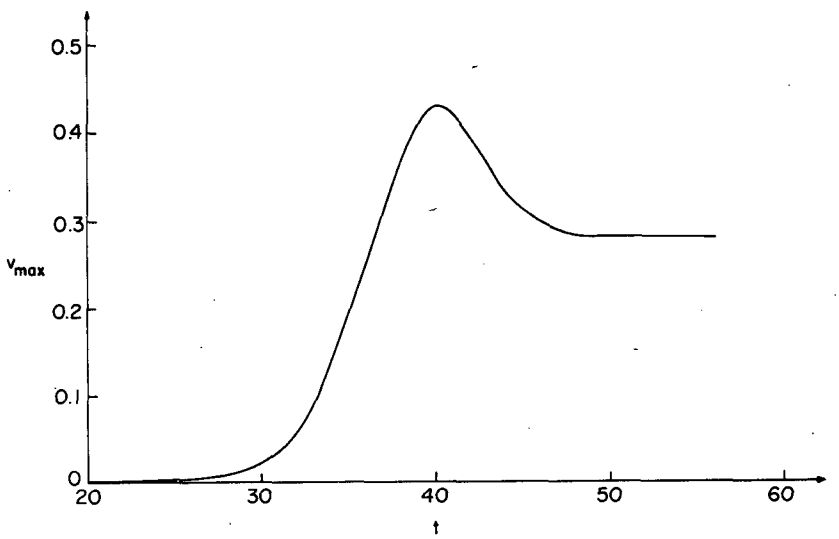

FIG. 7. The maximum surface value of the spanwise velocity component as a function of time. $v_{\max} = \max_y v(y,0,t)$.

$$v_R = v^n_{i+1,j} + v^n_{i,j}, \quad v_L = v^n_{i,j} + v^n_{i-1,j},$$
$$w_R = w^n_{i,j+1} + w^n_{i,j}, \quad w_L = w^n_{i,j} + w^n_{i,j-1},$$
$$S = \begin{cases} 1, & \text{for } \mathrm{Pr} \geq 1 \\ \mathrm{Pr}, & \text{for } \mathrm{Pr} < 1. \end{cases}$$

The field was scanned to determine the largest allowable Δt satisfying the stability requirement (34) and then a convenient constant value of Δt was used. After every time step, comparisons were made to ensure that this value did not exceed the current stable value of Δt.

The perturbation is introduced at any time by taking

$$\left.\begin{aligned} u^n_{i,j} &= \bar{u}^n_j(1 + 10^{-3}\sin\gamma i) \\ v^n_{i,j} &= w^n_{i,j} = \theta^n_{i,j} = 0 \end{aligned}\right\}, \tag{35}$$

where $\bar{u}^n_j$ is the shear flow (17) evaluated at time $t = n\Delta t$ and at grid points $y = (i - 1)\Delta y$, $z = -(j - 1)\Delta z$ ($j = 1$ being located at the surface $z = 0$) and γ is the perturbation wavenumber; typically we let $\gamma = m\pi/4$, m an integer. The sequence of computations is explicitly given by Paolucci (1979).

Here we point out that for our computations the cell Reynolds number, which is a measure of artificial diffusion, is defined by

$$\mathrm{Re}_c = \frac{|\mathbf{v}|\Delta}{\mathrm{La}},$$

where $\Delta = \Delta y = \Delta z$. It is observed that in all cases computed the maximum value of Re_c in the field was approximately 6; however, over most of the computational region its value was considerably less. We note that upwind differencing is not stability limited by a cell Reynolds number, but for formal second-order accuracy it is required that $\mathrm{Re}_c \leq 4$ (Roache, 1976). However, in practice, the requirement is not this stringent. Torrance (1968) in calculations of natural convection at high Grashof number (an equivalent of $\mathrm{Re} \approx 300$), showed that the second upwind differencing method results differed by less than 5% from a second-order solution. Runchal and Wolfshtein (1969) also used the second upwind differencing method to compute driven cavity flows. At a Reynolds number of 100, their 13×13 mesh gives a cell Reynolds number of ~ 20. Yet their results compare very favorably with a second-order solution in a 51×51 mesh.

5. Numerical results

Several numerical experiments were conducted, both in homogeneous water and in water with an initially uniform, statically stable temperature gradient. In Leibovich and Paolucci (1980a) we find these flows (for the particular Stokes drift to be adopted here) to be unstable for $\mathrm{La} < 0.66$ for homogeneous fluids; a statically stable initial density distribution reduces this critical Langmuir number, but for realistic values of the Richardson numbers, the stabilizing effect is slight. In L1, it is argued that under circumstances of interest in the ocean, the Langmuir number is expected to be small compared to unity, and probably in the range 0.001–0.01 or smaller. We have chosen to present results for $\mathrm{La} = 0.01$; this permits a numerical computation with acceptable spatial resolution, yet with sufficiently small La to be physically reasonable. It also permits a comparison with Leibovich and Radhakrishnan's (1977) solutions. The specific form of the Stokes drift is not expected to change the qualitative results found here.

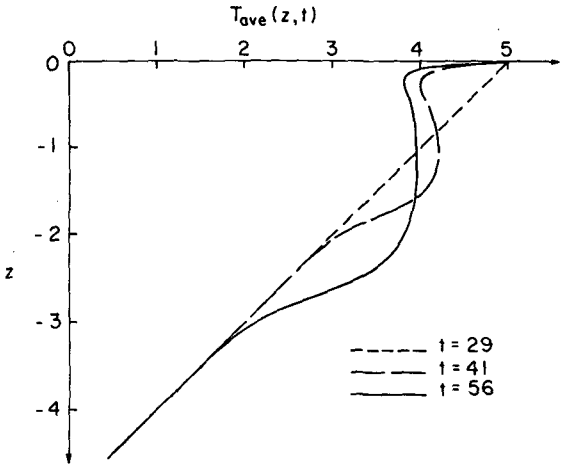

FIG. 8. Average temperature profile as a function of depth and time. The average is taken over the cell wavelength λ_c.

Clearly, our flows are highly unstable from the point of view of linear stability theory, and convection therefore always took place in the numerical simulations. In the experiments, the (dimensionless) width d of the computational domain, and the Richardson number Ri were varied.

With boundary conditions (31), convection is kinematically possible for wavelengths $\lambda_c = 2d/n$, $n = 1, 2, 3, \ldots$. Each wavelength λ_c involves two counterrotating vortices, each of which we call a "cell", and for odd values of n, the computational field of width d will contain an odd number of cells. For a fixed width d, an even or odd number of cells evolve if the vertical vorticity associated with the initial perturbation (35) has an odd or even number of zeros in the interior of the interval $(0,d)$, i.e., if the initial conditions specify an even or odd number of cells, although the ultimate number of cells to evolve is not necessarily determined by the initial perturbation.

In this section, we present the results of two of these numerical experiments. In both we take

$$u_s = 2e^{2z}, \quad \mathrm{Pr} = 6.7, \quad \mathrm{Ri} = 10^{-1}.$$

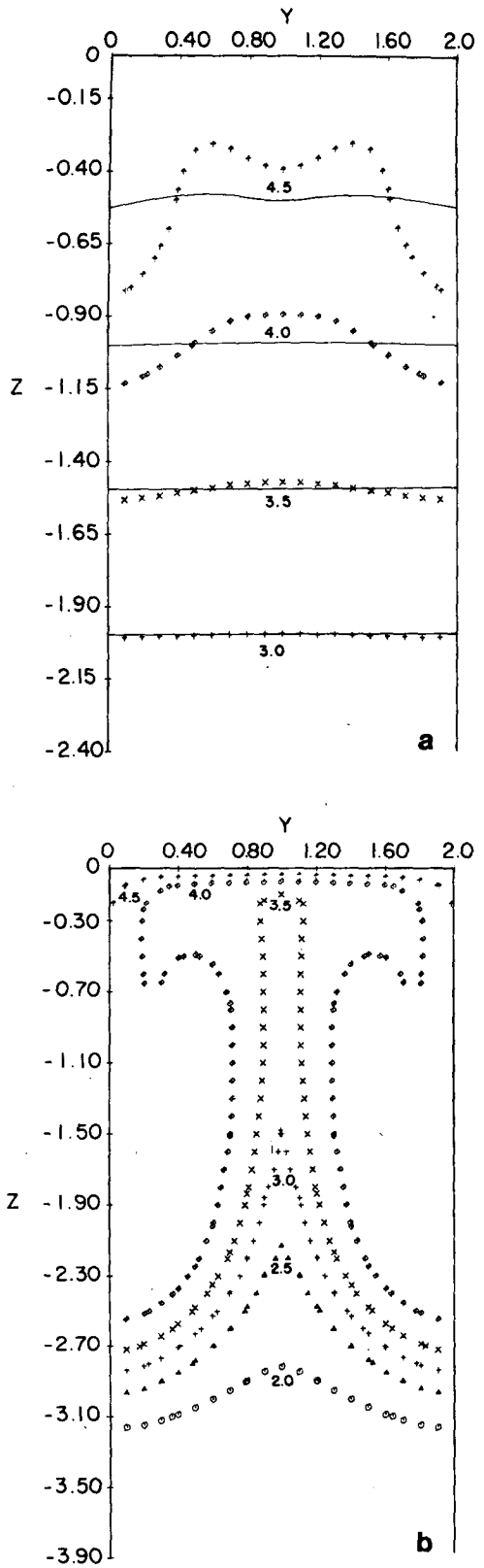

FIG. 9. Map of isotherms $T = \bar{T} + \theta$. At $z = 0$, T and $\bar{T}$ are fixed at $T = \bar{T} = 5.0$. (a) Solid lines, isotherms at $t = 29$; symbols, isotherms at $t = 35$; (b) isotherms at $t = 56$.

The dimensionless Stokes drift corresponds to straight-crested monochromatic surface waves, but it is unlikely that the specific form of u_s matters much as long as it decays with depth on a scale comparable to the length scale κ^{-1}. The Prandtl number is accurate for water based on molecular diffusivities; it is also a reasonable value when based on eddy diffusivities. A Richardson number, defined by (14), of 10^{-1} is a typical value for the ocean as we shall show in Section 6.

The two experiments described here lead to convection with dimensionless wavenumbers $\lambda_c = 2$ and $\lambda_c = 4$. Leibovich and Paolucci (1980a) expect the linearly most unstable motion for La = 0.01 and Ri = 10^{-1} to occur for $\lambda_c \approx \pi/2$. Thus, the case $\lambda_c = 2$ is not too far from the mode preferred by linear theory.

a. Numerical experiment leading to $\lambda_c = 2$

In all cases where the flow was unstable, it was observed that for some time the destabilizing effect was very slow, and then within a very short time the flow was totally destabilized giving rise to Langmuir cells. Afterward, there was a relaxation of the flow leading to a sort of "steady state." An explanation for this overshoot and subsequent relaxation has been given by Leibovich and Radhakrishnan (1977). The evolution of streamline patterns are illustrated in Figs. 1a–1c for a perturbation leading to $\lambda_c = 2$. In this case the shear flow was perturbed at time $t = 1$ with perturbation wavenumber $\gamma = \pi/4$. It is observed that as time evolves, the vortex centers move from near the surface to greater depths and are closer to the sides of the region than to the center, making downwelling stronger than upwelling motions. This is also clear from contours of the x vorticity component, which are not shown here.

The initial conditions involve four regions of alternating vorticity, or four initial cells. From the vorticity plots it can be seen that four cells persist at least until $t = 29$, but two are destroyed (between $t = 29$ and $t = 35$). This pattern is also reflected by the surface profiles of the velocity component u for various times, shown in Fig. 2. At all time levels shown in the figure, a peak in u occurs over convergence planes. In all the cases considered, peak speeds exceed minimum speeds by 25–40%. We see that for early times we have, in this case, three maxima and two minima corresponding to three downwelling and two upwelling regions. Eventually, we obtain downwelling regions next to the boundaries and upwelling at $y = 1$.

Vertical momentum transfer is obvious in the evolution of subsurface behavior of the horizontal average of u shown in Fig. 3. The presence of a viscous boundary layer next to the surface is also clear. The detailed spanwise distributions of u with

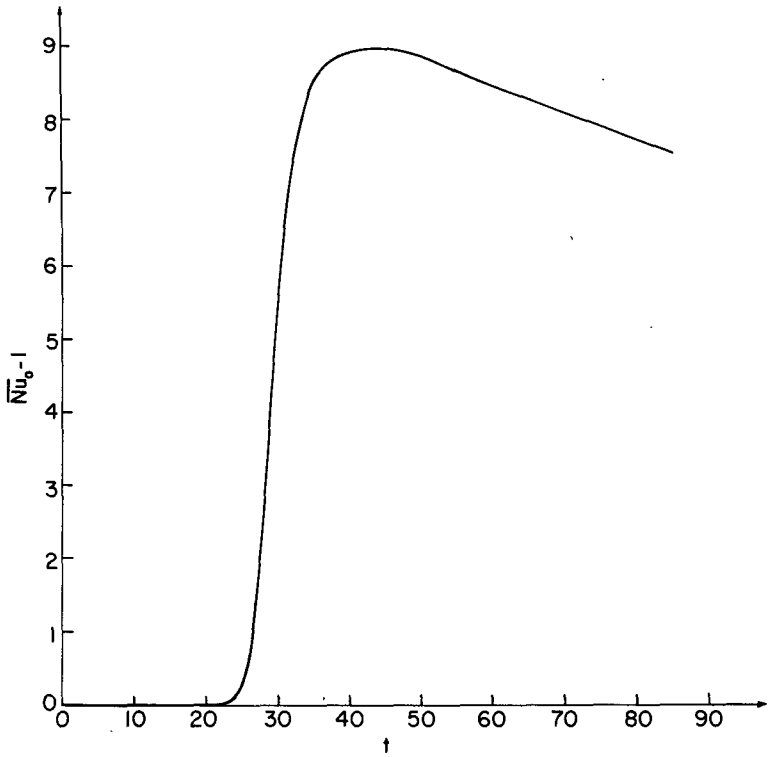

FIG. 10. Plot of the average heat transfer into the fluid due to convection. The average is taken over the cell wavelength λ_c.

depth and time are not shown here, but the corresponding profiles are shown for the $\lambda_c = 4$ example. The detailed profiles, in both the $\lambda_c = 2$ as well as the $\lambda_c = 4$ example, also illustrate the strong vertical momentum transfer.

Vertical velocities are plotted as functions of depth at planes of convergence and divergence in Fig. 4 for various times. Notice that the maximum upwelling speed occurs at a slightly lower depth than the downwelling speed and their depths progressively increase with time. The maximum speeds change very little with time after the velocity overshoot subsides as can be seen in Fig. 5. The numerical values for the maximum downwelling in all cases considered vary from ~50% to the same as the maximum surface values of u; note that the scaling (8) for the u and v components differ by a constant factor and so the ratio of numerical values does not indicate the ratio of actual velocities. For the largest values of time shown in the present case, downwelling exceeds maximum upwelling by ~25%.

The surface values of the spanwise velocity com-

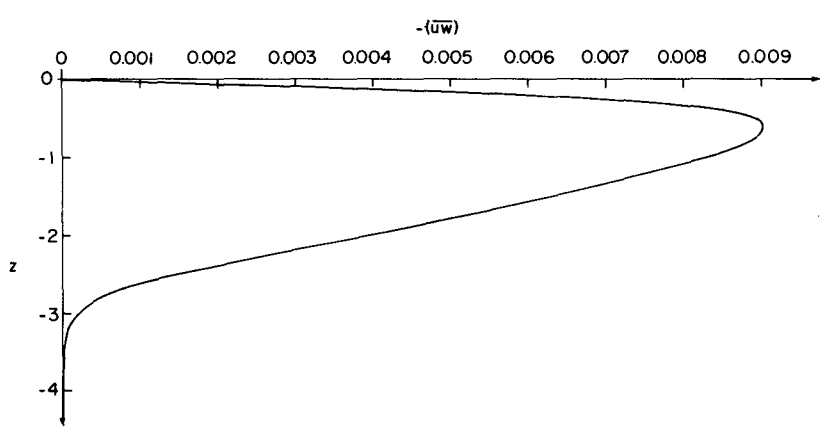

FIG. 11. Graph of the Reynolds stress versus depth at $t = 56$.

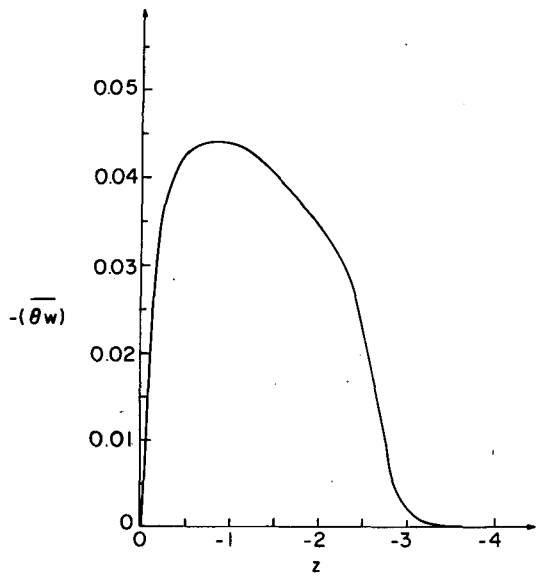

FIG. 12. Plot of the convection heat flux correlation as a function of depth at $t = 56$.

ponent v are shown in Figs. 6 and 7. By comparing values given in these figures with those in Figs. 4 and 5 it is seen that the maximum horizontal sweeping velocity for the largest times is ~30% lower than maximum downwelling. This remains approximately true in the other cases computed. The maximum value of spanwise velocity component is obtained between one-third and one-half the distance between downwelling and upwelling regions in all cases considered. In the present case it is located approximately at one-third the distance.

The mixed layer and a thermocline are clearly established in Fig. 8 where we show the temperature field, defined by (16), as it evolves from the initial conduction profile to a nearly uniform one at a later time. Notice the temperature inversion region below the surface and the presence of a thermal boundary layer. We do not show here the detailed variations of temperature with depth in planes at various spanwise locations since these figures are similar to those for $\lambda_c = 4$, which will be presented.

The magnitude of the mixing can be appreciated by observing the distortion of the isotherms shown in Figs. 9a and 9b. Warm fluid from the surface is transported down by the downwelling jet, while the colder fluid is brought to the surface in the upwelling region. It is clear, particularly from Fig. 9b, that cold water overlies warmer water. Of course, this is an instantaneous picture. The full nonlinear equations that we use include the usual nonlinear thermal convection equations as a subset; therefore, the evolution of thermally unstable configurations, when they arise in our flows, are properly traced in the course of the computations.

A plot of the heat transfer from the atmosphere to the ocean, averaged over one wavelength, is shown in Fig. 10, where the result is for the extended interval of time of $t = 85$. Again, the abrupt acceleration of the instability and the subsequent relaxation are evident from this figure.

The Reynolds stress $-(\overline{uw})$ is shown in Fig. 11 for the nondimensional time of 56. For the same value of time, we also show in Fig. 12 the thermal flux correlation $-(\overline{\theta w})$ associated with convection. The maxima of the above quantities occurs near the surface in the layer affected by u_s. In the mixed layer both Reynolds stress and heat flux decay, and become essentially zero at the bottom of the thermocline. Both correlations vary considerably in the mixed-layer region; however, it is expected (and can be seen in the case of $\lambda_c = 4$ to be presented later) that as time evolves, they will spread out to more constant values within the interior of the mixed-layer region.

A measure used to numerically define the depth to which the fluid is influenced by the convection is what we call the depth of influence (DOI). The DOI is defined as the depth at which the windward velocity component u decays to $<10^{-5}$ of its surface value, and both ξ and θ are $<10^{-4}$. The depths at which isotherms, Reynolds stress and heat flux correlation, respectively, were less than 10^{-6}, are considerably smaller than the DOI, and represent a more meaningful, though still arbitrary, measure of the depth influenced by the resulting cellular flow. The depths at which the Reynolds stress or heat flux exceed 10^{-6} both increase in time like $t^{1/3}$ after a temporary linear growth. This is in agreement with the results from the one-dimensional models of Niiler (1975) and deSzoeke and Rhines (1976).

b. Numerical experiment leading to $\lambda_c = 4$

For the same nondimensional parameters and perturbations leading to different cell wavelengths, we again observe the same qualitative features. An interesting case is offered by that leading to $\lambda_c = 4$. In this case the computational width was kept the same at $d = 2$, while the perturbation wavenumber was changed to $\lambda = \pi/2$. With this wavenumber, five cells initially exist. Only three remain at $t = 38$, the earliest time shown in Fig. 13. Eventually the middle of these three cells was destroyed by being squeezed by the two adjoining cells. Once this was accomplished, the two remaining cells, having circulations of the same sense, merged into one larger cell. Thus, in the end we obtain the flow pattern corresponding to a cell wavelength of 4.

The sequence of the events just described is clearly seen in the streamline plots shown in Figs. 13a–13d. The marked change from $t = 56$ to $t = 59$ results from a period of rapid growth at about this time similar to that occurring near $t = 30$ in the solution of Section 5a. It is observed that the cell is more

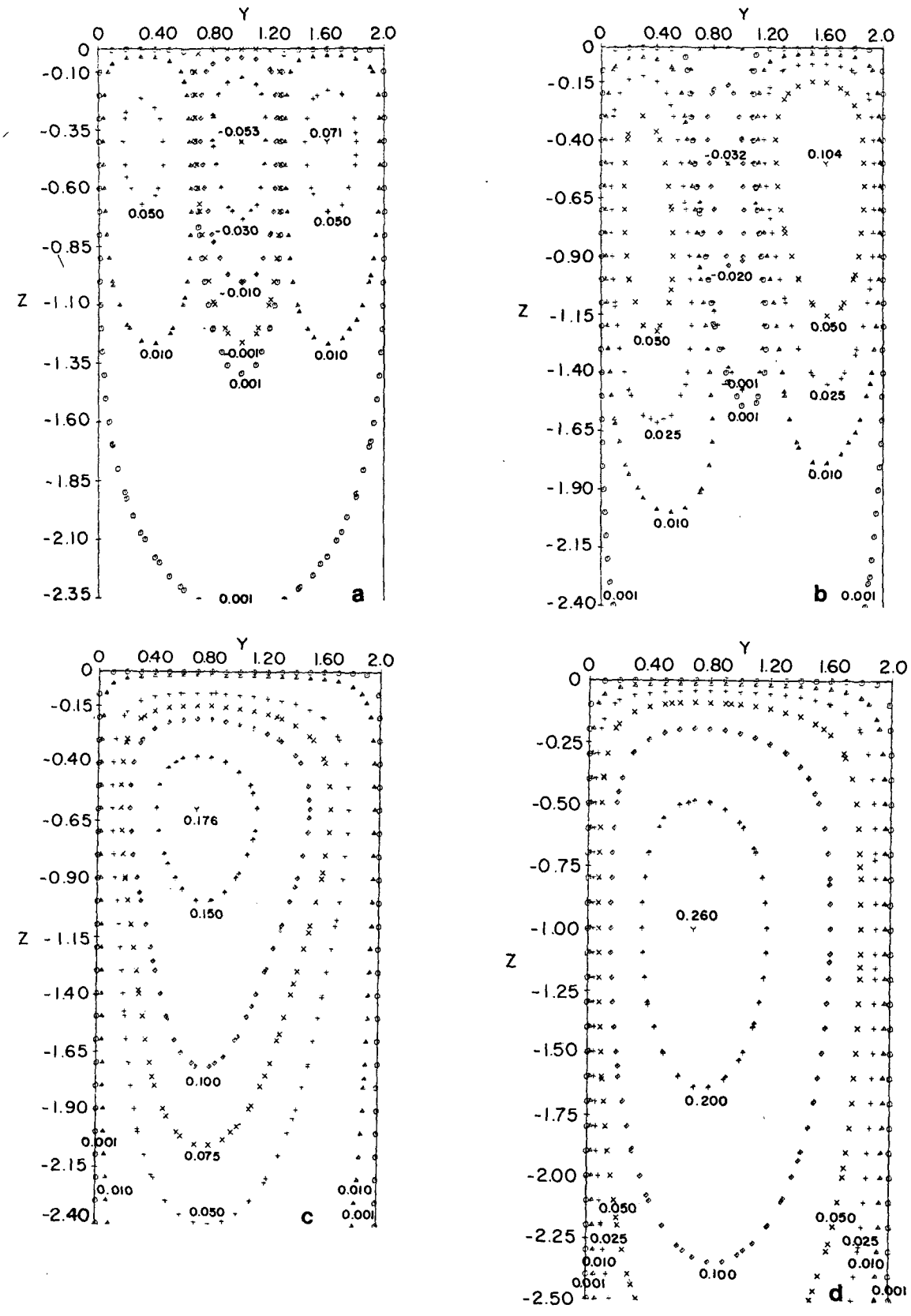

FIG. 13. Streamline patterns for $\lambda_c = 4$ at various times. The motion is clockwise in the middle cell and counterclockwise in the two end cells in (a) and (b). (a) $t = 38$; (b) $t = 44$; (c) $t = 56$; the motion is counterclockwise here and in (d); (d) $t = 59$.

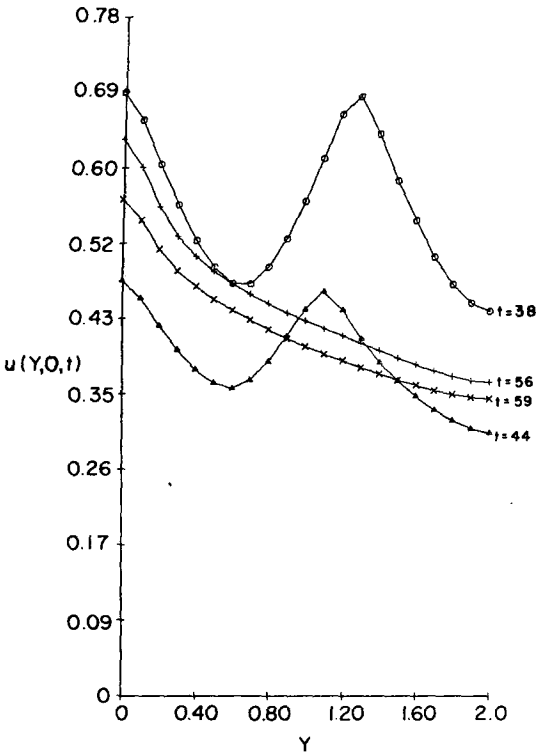

FIG. 14. The wind-directed current speed at the surface as a function of the spanwise coordinate y for different values of time.

asymmetric than in the previous case of $\lambda_c = 2$. From the above cases, as well as from other cases of λ_c for which computations were made, we conclude that as λ_c increases, the cells become more and more asymmetric. The difference between the surface windward velocity at the convergence zone and that at the divergence zone, and the difference between the downwelling and upwelling speeds, is therefore expected to increase. This pattern can be seen by comparing Figs. 2 and 4 with Figs. 14 and 15 where we display the wind-directed speed at the surface, and the vertical velocity at planes of convergence and divergence, respectively, for the present case of $\lambda_c = 4$. It can be observed that the relative speeds also increase with increasing λ_c.

Profiles of the wind-directed current speed as functions of depth and time at different y planes are given in Figs. 16a–16c. By looking at the average windward velocity profile shown in Fig. 16d, we see that we have a well-defined layer in which the momentum is mixed to a nearly uniform profile.

In Fig. 17, the surface values of the sweeping velocity component are plotted as a function of the y coordinate and time. As in the case $\lambda_c = 2$, it achieves a maximum at approximately one-third the distance from the converging zone to the diverging zone. The magnitude of this maximum is higher than for the case of $\lambda_c = 2$, as expected, and this trend remains true for other values of cell wavelength.

The effect of this flow field on the original thermal conduction solution is illustrated in Figs. 18 and 19. In Figs. 18a–18d we show the deformation of the isotherms. The presence of three cells is again apparent in Figs. 18a and 18b and becomes more complicated in Fig. 18c; however, by $t = 59$, we can clearly see in Fig. 18d the emergence of only one cell. Figs. 19a and 19b illustrate the temperature profiles at the downwelling and upwelling planes,

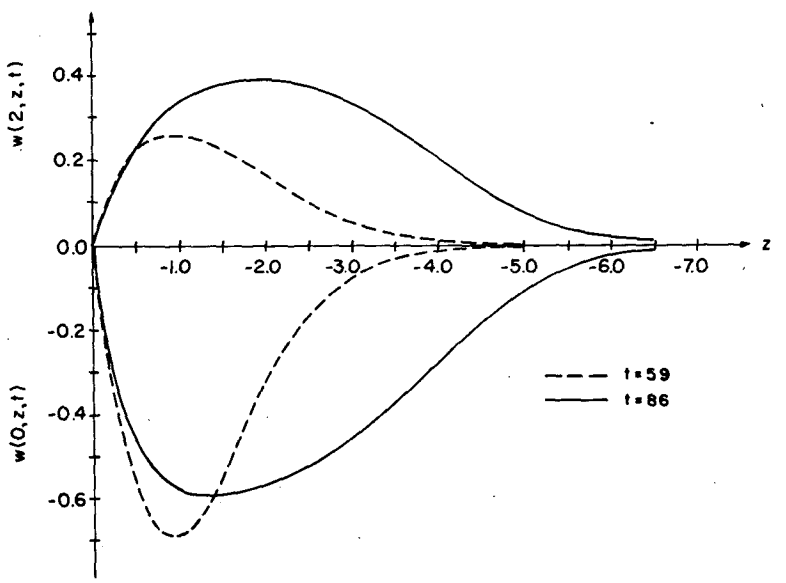

FIG. 15. Vertical velocity component as a function of depth at planes of convergence ($y = 0$) and divergence ($y = 2$) at various times.

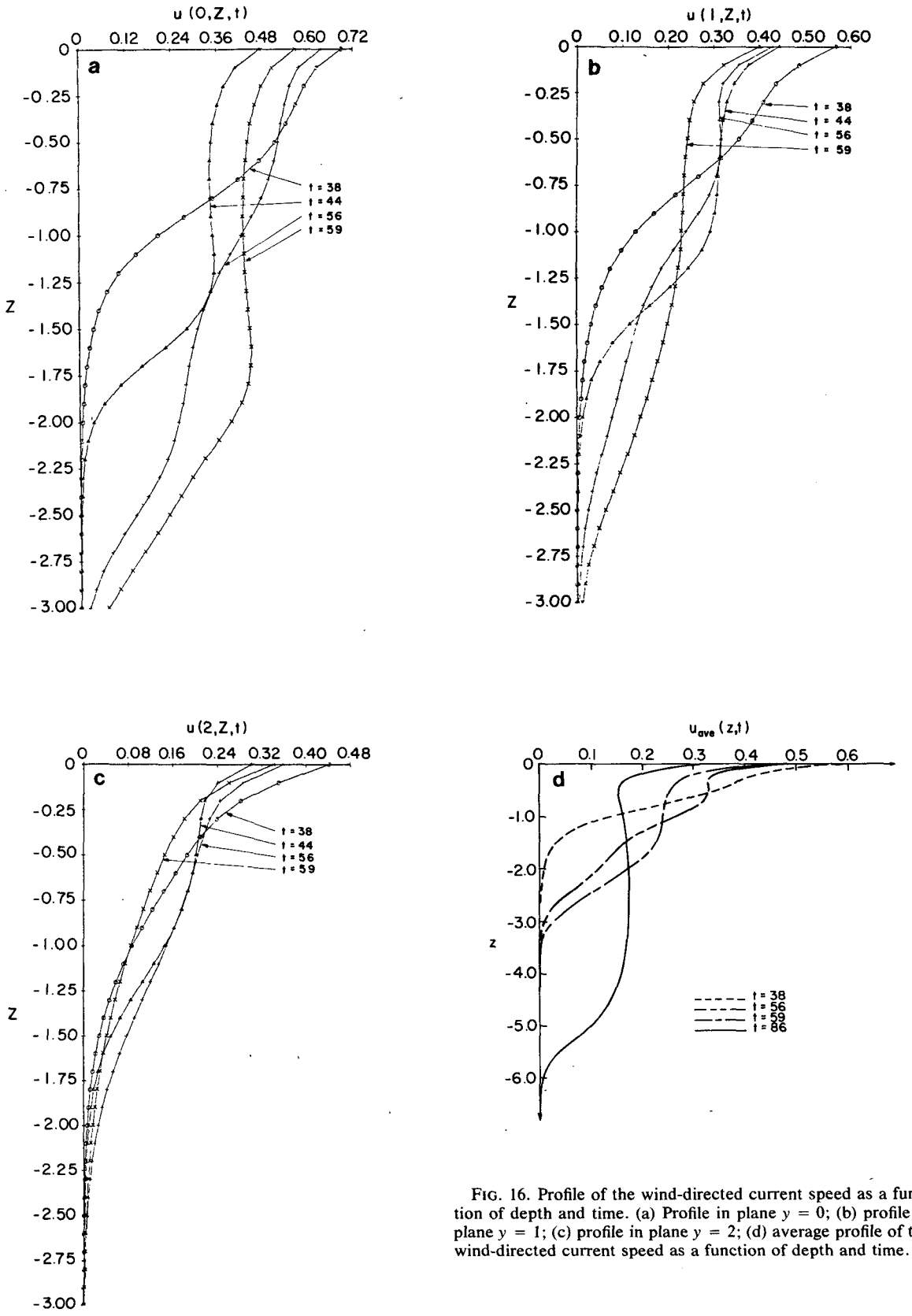

FIG. 16. Profile of the wind-directed current speed as a function of depth and time. (a) Profile in plane $y = 0$; (b) profile in plane $y = 1$; (c) profile in plane $y = 2$; (d) average profile of the wind-directed current speed as a function of depth and time.

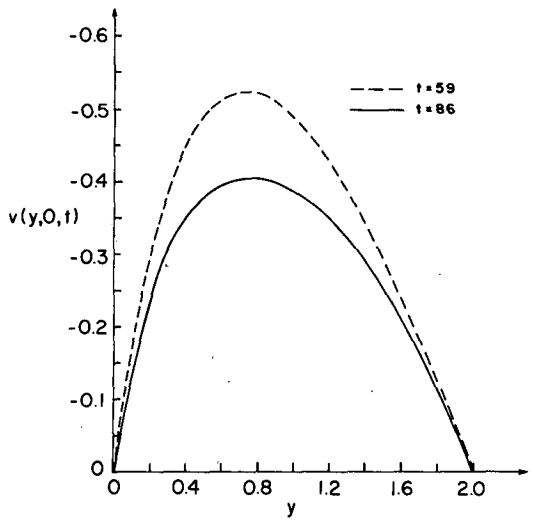

FIG. 17. Surface values of the spanwise (sweeping) velocity component as a function of the spanwise coordinate and time.

respectively. The average temperature profile in Fig. 19c shows that the mixed layer, besides having a nearly uniform current profile, is also almost isothermal in the vertical direction. However, in detail, both current and temperature, of course, are functions of the spanwise coordinate.

The Reynolds stress and heat flux correlation as functions of depth are shown in Figs. 20 and 21, respectively. As noted previously, both quantities spread out to nearly uniform profiles as time increases. Thus, we expect that both $-(\overline{uw})$ and $-(\overline{\theta w})$ become nearly uniform in the mixed-layer region.

In Fig. 22 we show a plot of the average heat transfer into the fluid due to convection. Although it has not reached some sort of equilibrium by $t = 86$, it is nevertheless evident that the heat flux is much higher than for the case of $\lambda_c = 2$ illustrated in Fig. 10. By looking at the heat flux for other cell wavelengths, we conclude that the rate of heat transfer increases with increasing distance between convergence planes.

In short, the qualitative result from our limited number of samples is that as the cells become bigger, the flow becomes more vigorous leading to higher speeds, greater mixing, and more sharply defined convergence and divergence regions.

6. Discussion and examples

The structural features of the Langmuir cells described in the previous section are remarkably similar to those computed by Leibovich and Radhakrishnan (1977). This is so despite the fact that the mechanism driving the convection differs in the two cases, and, despite the fact that a stable stratification exists here as opposed to the constant density case of the earlier study (this point is less important, since the realistic values of buoyancy selected here have only a weak stabilizing influence). In particular, the following qualitative features of reported field observations of LC are reproduced:

- Downwelling speeds are always greater than upwelling speeds.
- Warm water is pumped down in downwelling regions and cold water lifted in upwelling regions.
- The velocity component in the wind direction at the surface is greatest at lines of surface convergence and least at lines of divergence.

In addition, the LC are capable of creating and maintaining a mixed layer in which the averaged current and temperature are reasonably uniform from the surface to the LC "thermocline."

a. Example 1

To illustrate the results, we take a concrete and typical case and evaluate dimensional values of some quantities of interest. Let the friction velocity $u_* = 0.78$ cm s^{-1} which corresponds roughly to a wind speed $U \approx 10$ kt (5.1 m s^{-1}); take surface wave wavenumber κ and slope $\epsilon = a\kappa$ typical (Lissau, 1977) for this wind speed of $\kappa = 2.4 \times 10^{-3}$ cm^{-1} and $\epsilon = 0.073$, and evaluate the wave frequency from the deep water dispersion relation $\sigma = (gk)^{1/2}$; take $\nu_T = 24.8$ cm^2 s^{-1}, which is consistent with some empirical correlations at this wind speed; and take $\bar{T}' = 10^{-4}$ °C m^{-1} [or Brunt-Väisälä frequency $N = 4.47 \times 10^{-3}$ s^{-1} (Phillips, 1977)] as the temperature gradient in the ocean below the thermocline. These values correspond to La = 0.01 and Ri = 0.1, and we take the turbulent thermal diffusivity to be 3.7 cm^2 s^{-1} in order to give a Prandtl number of 6.7 as assumed in the numerical work.

With these parameters, the numerical solutions presented in the previous section may be adopted. To evaluate physical effects, we turn to the example of Section 5 for which $\lambda_c = 2$. The dimensional wavelength, or distance between convergence lines, in this case is 8.3 m. At the dimensionless time of 56, which corresponds to 66 min, we have the following results. The difference between the surface wind-directed velocity component at the convergence and divergence lines is 1.5 cm s^{-1}; the total drift at the convergence line is 11.4 cm s^{-1}, of which 6.8 cm s^{-1} is due to the Stokes contribution. The horizontally averaged total current at the surface is 10.4 cm s^{-1}. The maximum sweeping (i.e., spanwise or y directed) velocity component occurs 1.5 m from the convergence line and has a value there of 1.7 cm s^{-1}; the maximum upwelling and downwelling speeds are 1.8 and 2.4 cm s^{-1} and occur at depths of 3.5 and 2.9 m, respectively. The thermocline is approximately 11 m below the surface.

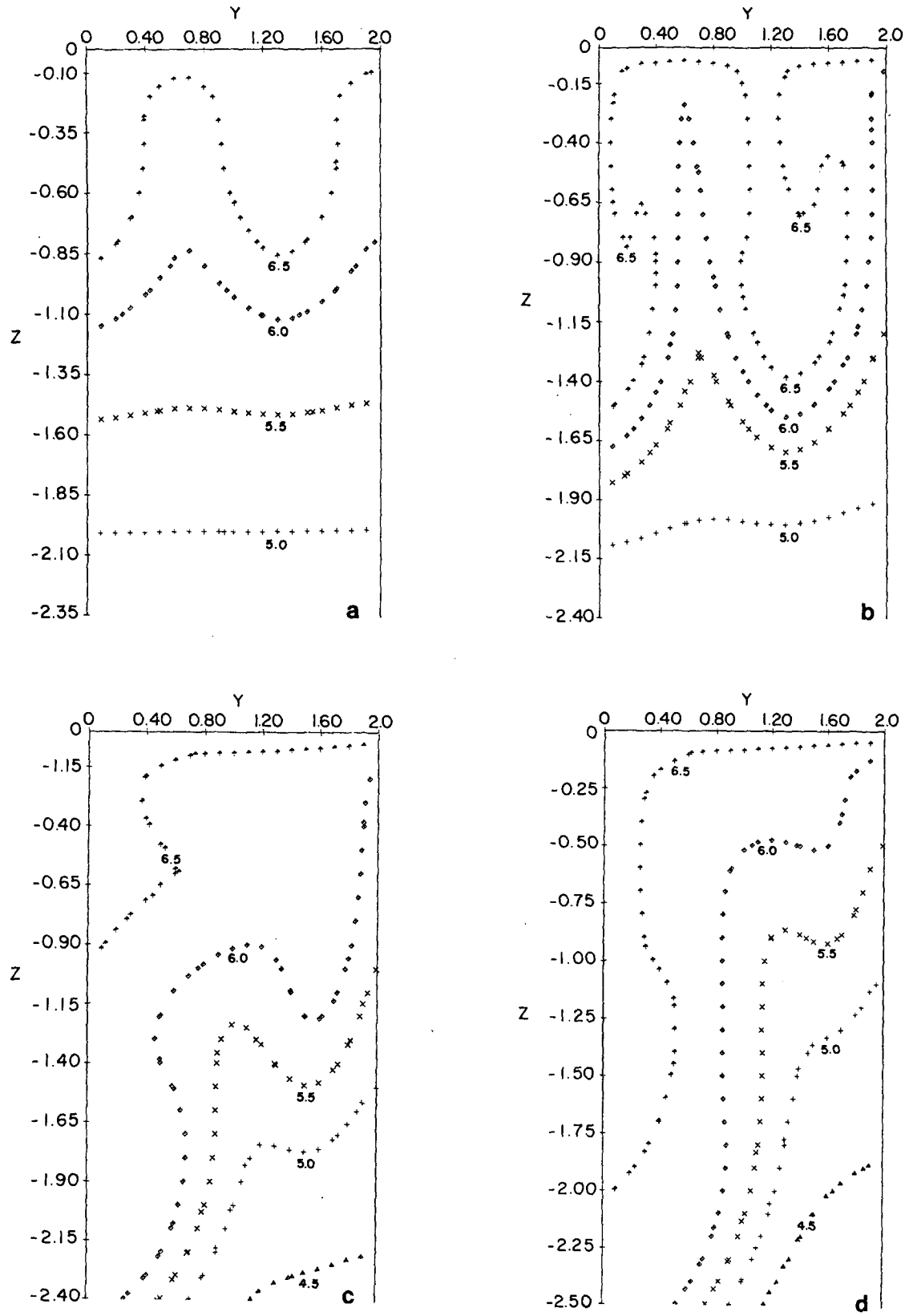

FIG. 18. Map of isotherms $T = \bar{T} + \theta$ for $\lambda_c = 4$ at various times. At $z = 0$, T and $\bar{T}$ are fixed at 7.0 (a) $t = 38$; (b) $t = 44$; (c) $t = 56$; (d) $t = 59$.

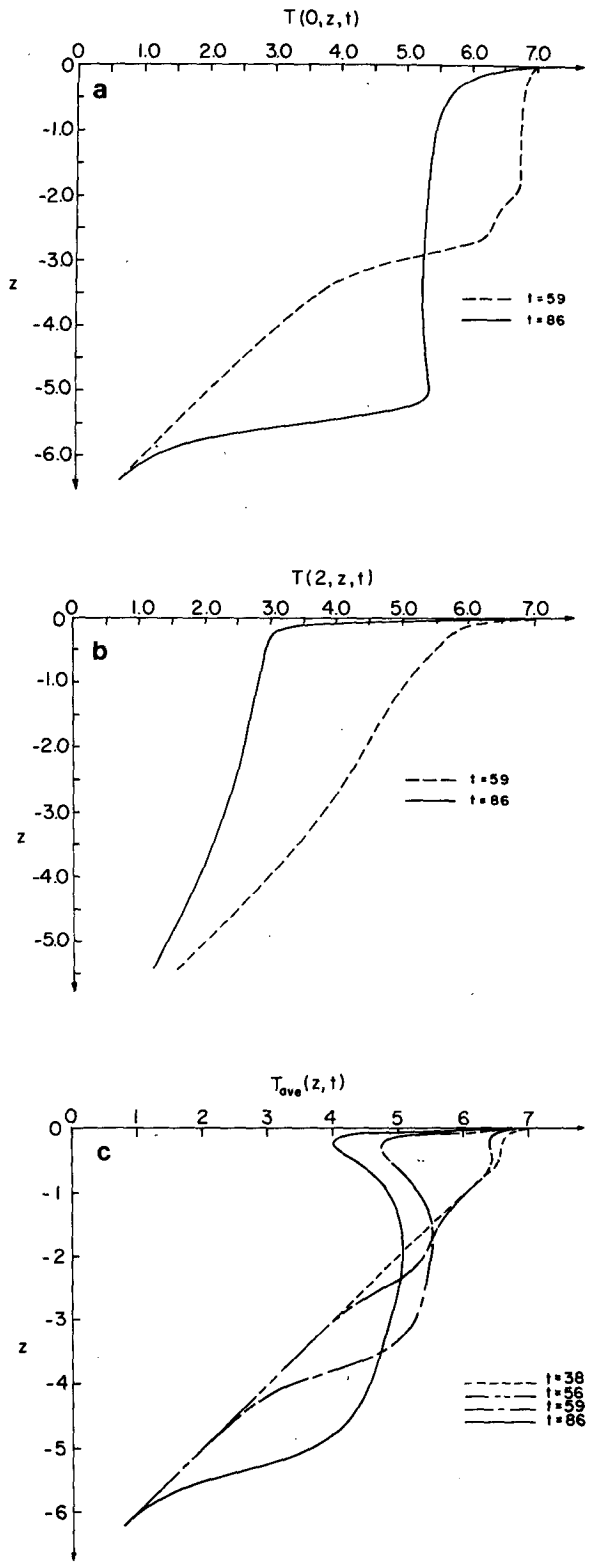

FIG. 19. Temperature profiles as a function of depth and time. Note that $T(0,z,t) = \bar{T}(z) + \theta(0,z,t)$ and we have taken $\bar{T}(0) = 7$. (a) Profile in plane $y = 0$, a downwelling location; (b) profile in plane $y = 2$, an upwelling location; (c) average temperature profile as a function of depth and time.

The mixing efficiency is a function of time; it is nearly zero for the first 30 min and reaches a maximum of 4.9 at 56 min. At 66 min, when the current system described above exists, $m = 4.2$.

b. Example 2

The mixing efficiency and the motion itself is clearly a lively function of sea state. Many physically plausible sets of input parameters (u_*, κ, σ, a, ν_T, $\bar{T}'$) can combine to give the two dimensionless parameters, La and Ri, that determine the mathematical solution to the problem. For example, the dimensionless solution for $\lambda_c = 2$, La = 0.01, Ri = 0.1, can also correspond to the physically reasonable set of parameters $\epsilon = 0.1$, $\sigma = 2.5\ s^{-1}$, $\kappa = 6.4 \times 10^{-3}$, $\nu_T = 8.25\ cm^2\ s^{-1}$, $u_* = 0.61\ cm\ s^{-1}$ and a Brunt-Väisälä frequency of $1.06 \times 10^{-2}\ s^{-1}$. The dimensionless time of 56 now corresponds to 28 min, and $\lambda_c = 2$ corresponds to a distance of 3.2 m between convergence lines. The thermocline is located ~4.2 m below the surface. The various speeds in the convective motion are comparable; the maximum value of $m = 7.3$ at 23.6 min, and has relaxed to 6.3 at 28 min.

We have focused attention up to this point on the case $\lambda_c = 2$ because it is close to the most unstable mode of linear theory. We recognize, however, that although this mode should dominate under marginally unstable conditions, there is no compelling reason why this is likely to be the case under the highly unstable conditions dealt with in this paper. In fact, in all our calculations, a cascade from smaller scales to the largest compatible with the computational domain d and the bias (toward an even or odd number of cells in d) imposed by the initial perturbation takes place. While our set of computed examples is too small for us to draw a conclusion from these observations, we point out the possibility that these tendencies may be characteristic.

c. Example 3

With this in mind, it is inappropriate to single out the $\lambda_c = 2$ case as an illustration, and we therefore describe the flow corresponding to the parameters in example 1, but for the motion with $\lambda_c = 4$. The time scale is as before, and we describe this flow at a dimensionless time of 59 which corresponds to 70 min. The distance between convergence lines is twice that of example 1, or 16.6 m, and the thermocline at this time remains at ~11 m below the surface (by 101 min, however, the thermocline has penetrated twice this depth). The difference between the surface wind-directed velocities at convergence and divergence lines is 2 cm s^{-1}; the total surface drift at the convergence line is 12.6 cm s^{-1}, of which, again, 6.8 cm s^{-1} is due to Stokes drift. The horizontally averaged current at the surface is ~12 cm s^{-1}. The

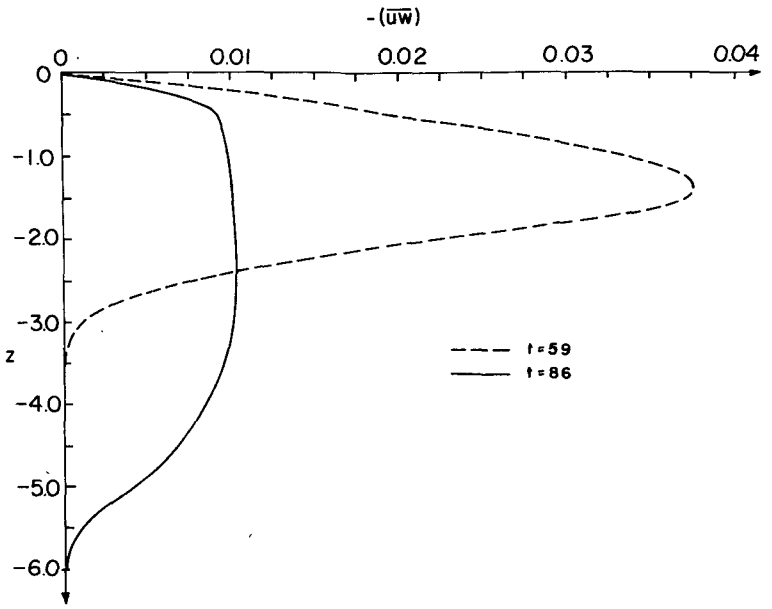

FIG. 20. Graph of the Reynolds stress versus depth at different times.

maximum sweeping velocity is 2.4 cm s^{-1} and occurs ~3 m from the convergence line. The maximum downwelling speed of 4 cm s^{-1} occurs ~3.8 m below the surface; the maximum upwelling of 1.5 cm s^{-1} occurs at a depth of ~4.2 m.

The mixing efficiency in this example is ~13 at 70 min, reflecting the very large heat fluxes shown in Fig. 21.

7. Concluding remarks

The character, length scale and strength of the motions calculated in this paper are, to the best of our knowledge, in agreement with field observations of the phenomenon. For instance, the situation in example 3 corresponds to a wind speed of ~5 m s^{-1}, and the maximum vertical speeds attained (at 70 min) are 4 cm s^{-1}. This is 0.8% of the wind speed, which corresponds well with observations (Scott *et al.*, 1969). The adjustable parameters in the theory are the turbulent momentum and heat diffusivities ν_T and α_T, the appropriate value to be taken for u_* and the Stokes drift. There is little that we can add to the discussion of Leibovich and Radhakrishnan (1977) concerning the eddy diffusivities. We should note here that we have tacitly assumed that u_* should be based on the full stress applied by the wind to the ocean surface. This, however, remains an uncertain assumption, particularly in the case of a developing sea, in which some of the momentum transferred to the ocean is radiated away by surface waves.

The formation of surface jets in the wind direction,

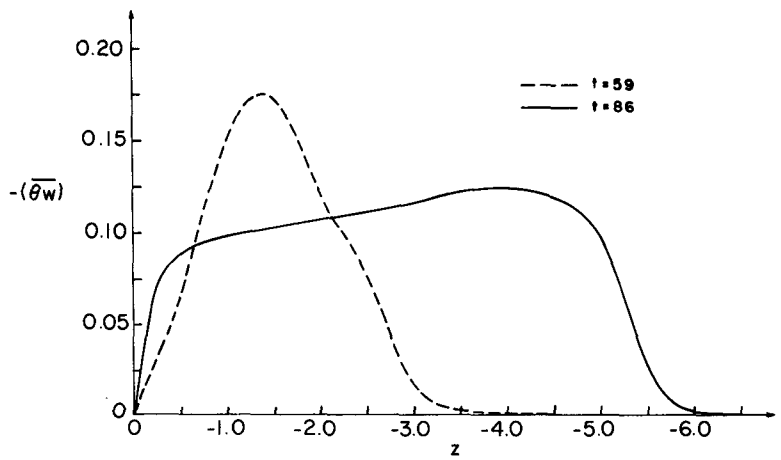

FIG. 21. Plot of the heat flux correlation as a function of depth at different times.

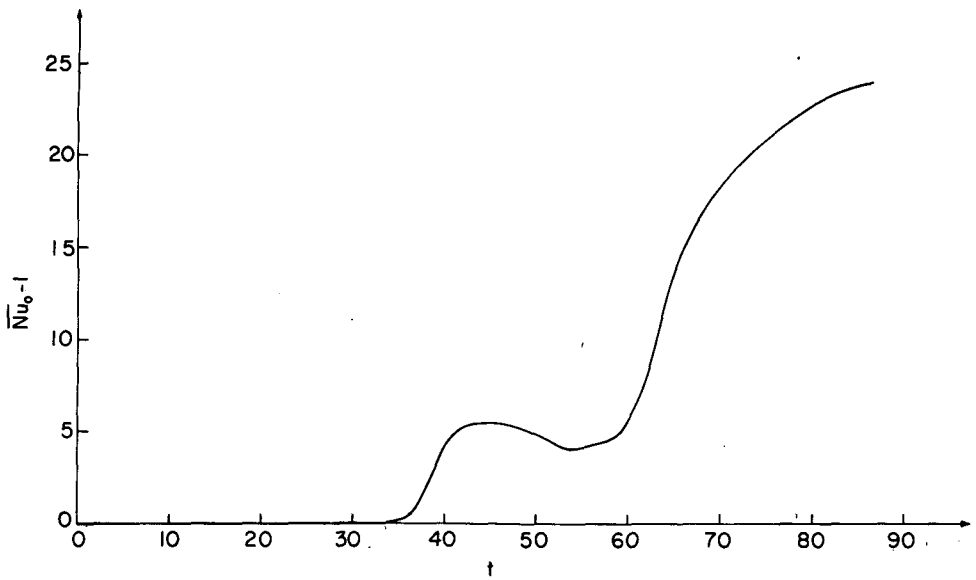

FIG. 22. Plot of the average heat transfer into the fluid. The average is over the cell wavelength.

discussed in Section 6 and evident in Figs. 2 and 14, is a well-known feature of observed Langmuir circulations. The physical mechanism of their formation according to the CL theory is the same one put forward by Langmuir (1938). Low momentum fluid brought to the surface at upwelling sites is accelerated by the applied wind stress as it is swept from upwelling to convergence zones. The speed (in the wind direction) attained by a fluid particle depends on the length of time it experiences the wind stress. As it approaches a convergence zone, the sweeping velocity decreases rapidly, and so the length of time a particle spends near the surface increases near convergence. Hence the more or less well-defined jet overlying convergences.

Our assumption of a fixed surface wave field, hence a time-independent Stokes drift, is not a restriction imposed by the theory. The theory accommodates a developing wave field, and the convective activity associated with such conditions can be calculated with equal ease.

Adrian Gill (private communication) has suggested that the inflection points in the horizontally averaged velocity profiles (Figs. 3 and 16d) may be subject to a shear-flow instability that could promote additional mixing localized near the bottom of the mixed layer. This kind of instability is filtered out of the present computations, since x-dependence is required for it. (I am indebted to Alex Craik for reminding me of Gill's comments.) Such an instability is a possibility, although it is important to keep in mind that the horizontally averaged flow differs considerably from the very complicated (non-parallel) flow that actually occurs near any given point.

Our computations suggest an energy cascade from small to large scales in agreement with the experiments of Faller and Caponi (1978). Furthermore, by comparing examples 1 and 3, corresponding to the same surface forcing, larger scales are more vigorous and mix more efficiently. Thus, it would appear that the strength of mixing by LC increases in time as the scale increases. It is important to remember, however, that the neglect of Coriolis acceleration (or a bottom) places a restriction on the interval of time for which the present model is valid. After a reasonable fraction (¼–½) of a pendulum day, Coriolis acceleration must be restored if continued calculations are to relate to the ocean. This, of course, entwines the Langmuir circulation motions with an Ekman layer spiral, as reported in field observations by Assaf *et al.* (1971). We are currently working on an extended scheme that will permit the calculation of these motions.

Acknowledgments. We would like to thank Adrian Gill for asking a question that helped in the preparation of the paper. Alex Craik also offered useful suggestions that led us to clarify a number of points, and we thank him for his interest. This work was supported by the National Science Foundation under Grant OCE 77-04482.

REFERENCES

Andrews, D. G., and McIntyre, 1978: An exact theory of nonlinear waves on a Lagrangian-mean flow. *J. Fluid Mech.*, **89**, 609–646.

Assaf, G., R. Gerard and A. L. Gordon, 1971: Some mechanisms of oceanic mixing revealed in aerial photographs. *J. Geophys. Res.*, **76**, 6550–6572.

Craik, A. D. D., 1970: A wave interaction model for the generation of windrows. *J. Fluid Mech.*, **41**, 801–821.

——, 1977: The generation of Langmuir circulations by an instability mechanism. *J. Fluid Mech.*, **81,** 209–223.

——, and S. Leibovich, 1976: A rational model for Langmuir circulations. *J. Fluid Mech.*, **73,** 401–426.

de Szoeke, R. A., and P. B. Rhines, 1976: Asymptotic regimes in the mixed-layer deepening. *J. Mar. Res.*, **34,** 111–116.

Faller, A. J., 1978: Experiments with controlled Langmuir circulations. *Science*, **201,** 618–620.

——, and E. A. Caponi, 1978: Laboratory studies of wind driven Langmuir circulations. *J. Geophys. Res.*, **83,** 3617–33.

Kato, H., and O. M. Phillips, 1969: On the penetration of a turbulent layer into stratified fluid. *J. Fluid Mech.*, **37,** 643–655.

Kenyon, K. E., 1969: Stokes drift for random gravity waves. *J. Geophys. Res.*, **74,** 6991–6994.

Langmuir, I., 1938: Surface water motion induced by wind. *Science*, **87,** 119–123.

Leibovich, S., 1977a: On the evolution of the system of wind drift currents and Langmuir circulations in the ocean. Part 1. Theory and averaged current. *J. Fluid Mech.*, **79,** 715–743.

——, 1977b: Convective instability of stably stratified water in the ocean. *J. Fluid Mech.*, **82,** 561–585.

——, 1980: On wave-mean flow interaction theories of Langmuir circulation. *J. Fluid Mech.* (in press).

——, and D. Ulrich, 1972: A note on the growth of small scale Langmuir circulations. *J. Geophys. Res.*, **77,** 1683–1688.

——, and K. Radhakrishnan, 1977: On the evolution of the system of wind drift currents and Langmuir circulations in the ocean. Part 2. Structure of the Langmuir vortices. *J. Fluid Mech.*, **80,** 481–507.

——, and S. Paolucci, 1980a: The instability of the ocean to Langmuir circulations. *J. Fluid Mech.* (in press).

——, and ——, 1980b: The energy stability of the Eulerian-mean motion in the upper ocean to three-dimensional perturbations. Submitted to *Phys. Fluids.*

Lissau, S., 1977: Ocean waves. *Oceanography: Contemporary Readings in Ocean Sciences,* R. G. Pirie, Ed., Oxford University Press, 424 pp.

Moen, J., 1978: A theoretical model for Langmuir circulations. Ph.D. thesis, University of Southampton, 235 pp.

Niiler, P. P., 1975: Deepening of the wind-mixed layer. *J. Mar. Res.*, **33,** 405–422.

Paolucci, S., 1979: Langmuir circulations as a convective instability mechanism and its effect on the ocean mixed layer. Ph.D. thesis, Cornell University, 218 pp.

Phillips, O. M., 1977: *The Dynamics of the Upper Ocean.* Cambridge University Press, 336 pp.

Roache, P. J., 1976: *Computational Fluid Dynamics.* Hermosa Publ., 434 pp.

Runchal, A. K., and M. Wolfshtein, 1969: Numerical integration procedure for the steady-state Navier-Stokes equations. *J. Mech. Eng. Sci.*, **11,** 445–453.

Scott, J. T., G. E. Myer, R. Stewart and E. G. Walther, 1969: On the mechanism of Langmuir circulations and their role in epilimnion mixing. *Limnol. Oceanogr.*, **14,** 493–503.

Swartztrauber, P., and R. Sweet, 1975: Efficient Fortran subprograms for the solution of elliptic partial differential equations. NCAR Tech. Note IA-109, 139 pp.

Turner, J. S., 1973: *Buoyancy Effects in Fluids.* Cambridge University Press, 367 pp. (see p. 300).

Torrance, K. E., 1968: Comparison of finite-difference computations of natural convection. *J. Res. Nat. Bur. Std.*, **72B,** 281–301.